



HAL
open science

Structural Effects of Anomalous Current Densities on Manganese Hexacyanoferrate for Li-Ion Batteries

Angelo Mullaliu, Stéphanie Belin, Lorenzo Stievano, Marco Giorgetti, Stefano
Passerini

► **To cite this version:**

Angelo Mullaliu, Stéphanie Belin, Lorenzo Stievano, Marco Giorgetti, Stefano Passerini. Structural Effects of Anomalous Current Densities on Manganese Hexacyanoferrate for Li-Ion Batteries. Applied Sciences, 2020, 10 (21), pp.7573. 10.3390/app10217573 . hal-02981315

HAL Id: hal-02981315

<https://hal.science/hal-02981315>

Submitted on 27 Oct 2020

HAL is a multi-disciplinary open access archive for the deposit and dissemination of scientific research documents, whether they are published or not. The documents may come from teaching and research institutions in France or abroad, or from public or private research centers.

L'archive ouverte pluridisciplinaire **HAL**, est destinée au dépôt et à la diffusion de documents scientifiques de niveau recherche, publiés ou non, émanant des établissements d'enseignement et de recherche français ou étrangers, des laboratoires publics ou privés.

Article

Structural Effects of Anomalous Current Densities on Manganese Hexacyanoferrate for Li-Ion Batteries

Angelo Mullaliu ^{1,2}, Stéphanie Belin ³, Lorenzo Stievano ^{4,5}, Marco Giorgetti ^{6,*}
and Stefano Passerini ^{1,2,*}

¹ Helmholtz Institute Ulm (HIU), Helmholtzstrasse 11, 89081 Ulm, Germany; Angelo.mullaliu@kit.edu

² Karlsruhe Institute of Technology (KIT), P.O. Box 3640, 76021 Karlsruhe, Germany

³ Synchrotron SOLEIL, L'orme des Merisiers, BP 48 Saint Aubin, 91192 Gif-sur-Yvette, France; stephanie.belin@synchrotron-soleil.fr

⁴ Institute Charles Gerhardt Montpellier (ICGM), University of Montpellier, ENSCM, CNRS, 34095 Montpellier, France; lorenzo.stievano@umontpellier.fr

⁵ Réseau sur le Stockage Electrochimique de l'Energie (RS2E), National Centre for Scientific Research (CNRS), 80039 Amiens, France

⁶ Department of Industrial Chemistry "Toso Montanari", University of Bologna, Viale Risorgimento 4, 40136 Bologna, Italy

* Correspondence: marco.giorgetti@unibo.it (M.G.); stefano.passerini@kit.edu (S.P.)

Received: 4 October 2020; Accepted: 26 October 2020; Published: 27 October 2020

Abstract: A battery management system (BMS) plays a pivotal role in providing optimal performance of lithium-ion batteries (LIBs). However, the eventual malfunction of the BMS may lead to safety hazards or reduce the remaining useful life of LIBs. Manganese hexacyanoferrate (MnHCF) was employed as the positive electrode material in a Li-ion half-cell and subjected to five cycles at high current densities ($10 \text{ A g}_{\text{MnHCF}}^{-1}$) and to discharge at $0.1 \text{ A g}_{\text{MnHCF}}^{-1}$, instead of classical charge/discharge cycling with initial positive polarization at $0.01 \text{ A g}_{\text{MnHCF}}^{-1}$, to simulate a current sensor malfunctioning and to evaluate the electrochemical and structural effects on MnHCF. The operando set of spectra at the Mn and Fe K-edges was further analyzed through multivariate curve resolution analysis with an alternating least squares algorithm (MCR-ALS) and extended X-ray absorption fine structure (EXAFS) spectroscopy to investigate the structural modifications arising during cycling after the applied electrochemical protocol. The coulombic efficiency in the first cycle was dramatically affected; however, the local structural environment around each photo absorber recovered during charging. The identification of an additional spectral contribution in the electrochemical process was achieved through MCR-ALS analysis, and the Mn-local asymmetry was thoroughly explored via EXAFS analysis.

Keywords: prussian blue analog; manganese hexacyanoferrate; MCR-ALS; XAFS; EXAFS; li-ion batteries; battery management system

1. Introduction

Lithium-ion battery (LIB) technology has experienced tremendous development over the last decades to meet society's energy requirements [1,2]. The advancement of LIBs is also related to the challenging tasks of decreasing greenhouse gas emissions and meeting the Sustainable Development Goals set in 2015 by the United Nations General Assembly [3]. Performance, cost, and safety are key features for promising LIB candidates [4]. However, safety concerns due to the presence of high-energetic materials and flammable components, fragility, and aging may restrict the use of LIBs and reduce the remaining useful life [5]. Within this context, an efficient and smart battery management

system (BMS) is of uttermost importance to guarantee the optimal performance of LIBs [6]. Nevertheless, the malfunction of the sensors on which the BMS relies, for instance, current sensors, may lead to hazardous consequences [7].

In this study, we evaluate the structural and chemical effects of the improper application of a high current density to a positive electrode material. The material under investigation is sodium-rich manganese hexacyanoferrate (MnHCF), a member of the Prussian blue analogs (PBAs) family, which appear promising for large-scale energy storage applications because of their ease of synthesis, low-cost, and earth abundance [8,9]. PBAs have also been demonstrated to be robust host materials; therefore, the stability and lifetime of the batteries may be enhanced [10]. MnHCF features a high specific capacity based on the redox activity at two species, i.e., Mn and Fe, and displays a large local structural effect following the Mn(II) oxidation to the Jahn-Teller (JT) active Mn(III) (Mn-N equatorial bond lengths are contracted by 10%) [11,12], which is, however, buffered in the long-range by the PBA open-framework. Indeed, MnHCF shows a non-cooperative JT effect and low volume change (2% only) during cycling [13].

Here, the applied protocol causes the formation of an additional spectral component compared to the previous study [12], as retrieved by multivariate curve resolution analysis with an alternating least squares algorithm (MCR–ALS). Although the loss in coulombic efficiency in the first cycle is drastic, the local structure analyzed by X-ray absorption fine structure (XAFS) spectroscopy is not significantly affected at the full state of charge and underlines the fair structural stability of the host, even after the applied electrochemical protocol.

2. Materials and Methods

Synthesis, characterization, and electrode preparation. Sodium-rich manganese hexacyanoferrate (MnHCF) was synthesized, characterized, and processed for electrode use, as previously reported [11]. The chemical formula of the synthesized material can be expressed as $\text{Na}_{1.9}\text{Mn}_{1.1}\text{Fe}(\text{CN})_6$. The electrode slurry consisted of the active material (MnHCF, 85 wt%), the conductive agent (Super C65, IMERYS, 10 wt%), and the binder (polyvinylidene difluoride, PVDF; Solef 6020, Solvay Polymerspecialties, 5 wt%). The areal loading of the electrodes had a Student's *t*-distribution of $2.47 \pm 0.04 \text{ mg}_{\text{MnHCF}} \text{ cm}^{-2}$, considering a population of 24 electrodes, and a confidence interval equal to 0.95. The final electrodes were extensively dried at 120 °C under vacuum (10^{-6} bar) for 24 h and finally stored in an Ar-filled glove box. For the detailed description of the synthesis, the physicochemical characterization, and the electrode processing, please refer to reference [11].

Operando XAFS measurements and data analysis. A suitable electrochemical cell for in situ experiments, described in detail elsewhere [14], was used for the XAFS measurements. A large piece of lithium metal foil was used as the negative electrode, while the MnHCF-based electrode was used as the positive electrode. LP30, i.e., 1.0 M LiPF_6 dissolved in a 1:1 volumetric mixture of ethylene carbonate and dimethyl carbonate (EC/DMC = 50/50 *v/v*), was adopted as the electrolyte solution. The positive electrode, glass fiber separator, and negative electrode were stacked and assembled under inert atmosphere in an Ar-filled glovebox. Galvanostatic cycling with potential limitation (GCPL) was conducted by considering 1C current rate equal to 150 mA h g^{-1} . The operando experiment was performed during one galvanostatic cycle at C/15 current rate (corresponding to a current density equal to $0.01 \text{ A g}_{\text{MnHCF}}^{-1}$), starting with the charge and by recording a full set of spectra from number 4 to number 123.

Before the operando experiment, the cell was subjected to an anomalous cycle test, consisting of five cycles with current density set at $\pm 10 \text{ A g}_{\text{MnHCF}}^{-1}$ (i.e., 67 C), to simulate BMS malfunctioning and ill-usage of the device, followed by a discharge with current density equal to $-0.1 \text{ A g}_{\text{MnHCF}}^{-1}$ (see Figure S1) [11,12].

XAFS spectra were recorded at the ROCK (Rocking Optics for Chemical Kinetics) beamline of the SOLEIL synchrotron [15]. Spectra were alternately collected from 6380 eV to 7080 eV and from 7000 eV to 7969 eV, i.e., around the Mn and Fe K-edges, respectively. The energies were calibrated by assigning the first inflection points of the spectra of manganese and of iron metal to 6539 and 7112 eV, respectively. XAFS data pre-treatment was carried out using ATHENA graphical utility [16]. The

normalized XAFS spectra were further analyzed using a chemometric approach, implying a combination of principal component analysis (PCA) with Multivariate Curve Resolution—Alternating Least Square (MCR-ALS) using a specifically developed toolbox in MATLAB [17] to retrieve mathematically the pure spectral components and the concentration profile plots from the experimental spectroscopic matrix. This analytical approach is described in detail in reference [18]. The extended X-ray absorption fine structure (EXAFS) analysis was performed using the GNXAS package [19,20], which is based on the decomposition of the EXAFS signals into a sum of two-body $\gamma^{(2)}$, three-body $\gamma^{(3)}$, and four-body $\gamma^{(4)}$ multiple scattering (MS) terms [21]. Since Fe-C-N-Mn chains feature angles close to 180° , the actual number of parameters used to define the three-body and the four-body peaks was reduced by symmetry. More details on the use of parameter correlation in the four-body term are out of the aim of the present work and can be found in references [22,23]. Data analysis was performed by minimizing a χ^2 -like residual function that compares the theoretical (model) signal, $\mu_{\text{mod}}(E)$, to the experimental one, $\mu_{\text{exp}}(E)$. The phase shifts for the photo absorber and backscattered atoms were calculated starting from the structure reported by Song et al. [24], according to the muffin-tin approximation and allowing a 10% overlap between the muffin-tin spheres. The Hedin-Lundqvist complex potential [25] was used for the exchange-correlation potential of the excited state. The core-hole lifetime, Γ_c , was fixed to the tabulated value [26] and was included in the phase shift calculation.

3. Results

3.1. Electrochemistry

Figure 1 compares the electrochemical charge-discharge behavior of the MnHCF electrode after the anomalous charge-discharge procedure with that recorded in the previous study [11] (blue curve). The reference electrode behavior (blue curve) reflects the typical charge/discharge curve of MnHCF. Starting from the open circuit potential (P^{ref} state of charge), the MnHCF de-sodiation in Li-based electrolytes occurs in a single extraction process at ~ 3.7 V within a narrow potential window up to C^{ref} state of charge. The following lithium insertion process (i.e., up to D^{ref} state of charge) takes place in two steps at ~ 3.6 and ~ 3.4 V (cf. ref. [11]). The charge-discharge behavior of the MnHCF electrode subjected to an anomalous charge-discharge procedure (red curve) displays significant changes compared to the typical profile of a pristine electrode. The charge starts at D_0 , showing a multistep ion de-insertion of both Li- and Na-ions, occurring in a larger voltage window (~ 1 V). Although a partial Li^+ uptake occurs upon the discharge at $0.1 \text{ A g}_{\text{MnHCF}}^{-1}$ (cf. Figure S1 in Supplementary Information), the large specific capacity displayed during charge (up to the point of C_1) cannot be exclusively explained by considering the ion-release process, but it could be due to the decomposition of the electrolyte solution in the last plateau above 4.1 V. In the following discharge process, a lower capacity is achieved (D_1 state of charge), resulting in a coulombic efficiency value of 63% (red curve), i.e., substantially lower than the 97% achieved by the pristine MnHCF electrode (blue curve). Therefore, the first five cycles at 67 C produced a notable loss of reversibility in the material performance in spite of the small charge-discharge capacities involved.

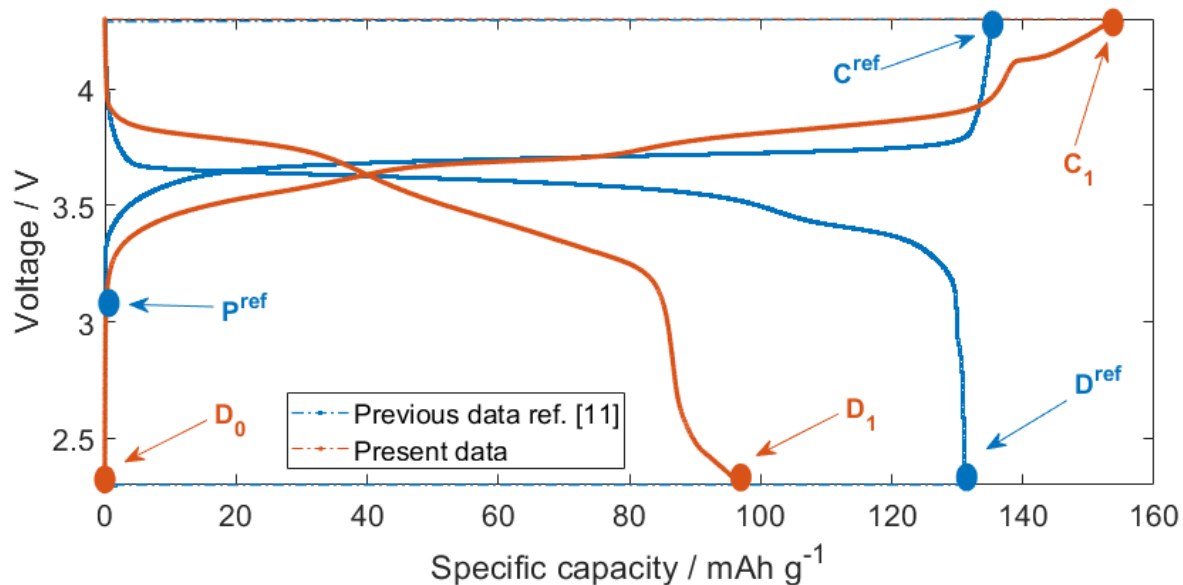


Figure 1. Voltage profiles upon galvanostatic charge-discharge of a manganese hexacyanoferrate (MnHCF) electrode subjected to anomalous pre-cycling (red curve). For comparison, the behavior of a pristine electrode (data from ref. [11]) is also shown (blue curve). Also shown is the labeling of a few selected states of charge (see text).

3.2. X-ray Absorption Near Edge Spectroscopy (XANES)

Operando Mn and Fe K-edge XANES spectra for the electrode at D_0 , C_1 , and D_1 states of charge are presented in Figure 2. The high variability in the Mn K-edge spectral shape and the low modifications occurring at the Fe K-edge are in line with previous work done on this material [11,12]. The Mn edge shifts towards higher energies during charge (C_1) as the Mn ions are oxidized from the divalent to the trivalent oxidation state. A similar trend is recorded also for the Fe edge (see Figure S2 for the magnified XANES portion), showing a higher threshold energy at C_1 as a result of the Fe oxidation during ion-release ($Fe^{II} \rightarrow Fe^{III}$). The ion-uptake during the following discharge (see spectra for D_1) triggers the reduction of both Mn and Fe centers, resulting in their spectral shapes almost coinciding with those seen at D_0 . We anticipate here that the difference between D_0 and D_1 spectra is relevant for the remaining part of the discussion revolving around the MCR-ALS analysis.

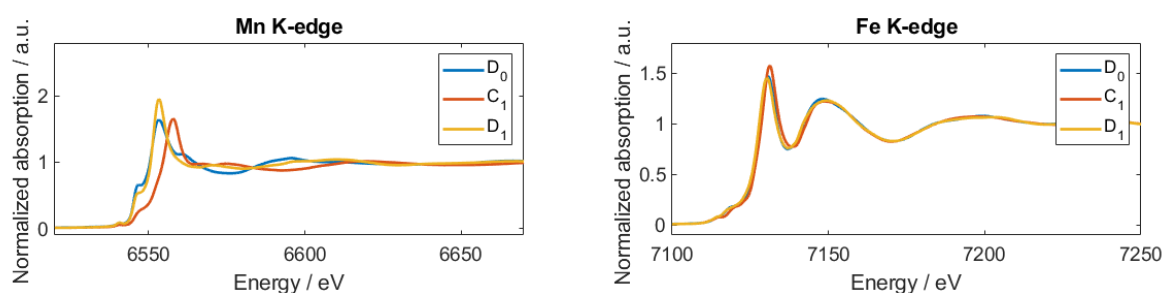


Figure 2. Spectra at the Mn and Fe K-edges for D_0 , C_1 , and D_1 states of charge.

To make a further comparison between the dataset recorded in this work and the earlier one [11], Figure 3 highlights the differences and analogies between the most relevant states of charge for both edges. The pristine state in Reference [11] (P^{ref}) and the discharged state (D_0) in the present dataset were used to compare the initial states of charge for MnHCF. As the Fe K-edge is modified only slightly, the differences between all the states of charge at the Fe edge do not appear significant (cf. Panels b, d, f), although Figure S3 underlines a non-perfect match between the considered pairs. On the other hand, the Mn K-edge shows major dissimilarities between pristine, charged, and discharged states (Panels a, c, and e, respectively). In particular, D_0 and D_1 significantly differ from P^{ref} and D^{ref} , respectively, while

the charged states, i.e., C_1 and C^{ref} , match fairly well. The D_0 and P^{ref} spectra are different, as expected (Panel a), due to the anomalous electrochemical pre-treatment. Despite the different initial states of charge, C_1 and C^{ref} appear almost identical (Panel c), giving further insight into the electronic and structural stability of MnHCF as the ion-release occurs. The consecutive discharge process gives as a result different spectral shapes, especially if the white line intensity is taken into consideration (Panel e); however, the signal modulation of the D_1 and D^{ref} samples coincides, as opposed to D_0/P^{ref} comparison (Panel a). The local structure around the Mn site is, therefore, not much affected by the anomalous pre-treatment, with the only exception being the very initial state not reflecting the much lower coulombic efficiency highlighted by the electrochemical results in Figure 1.

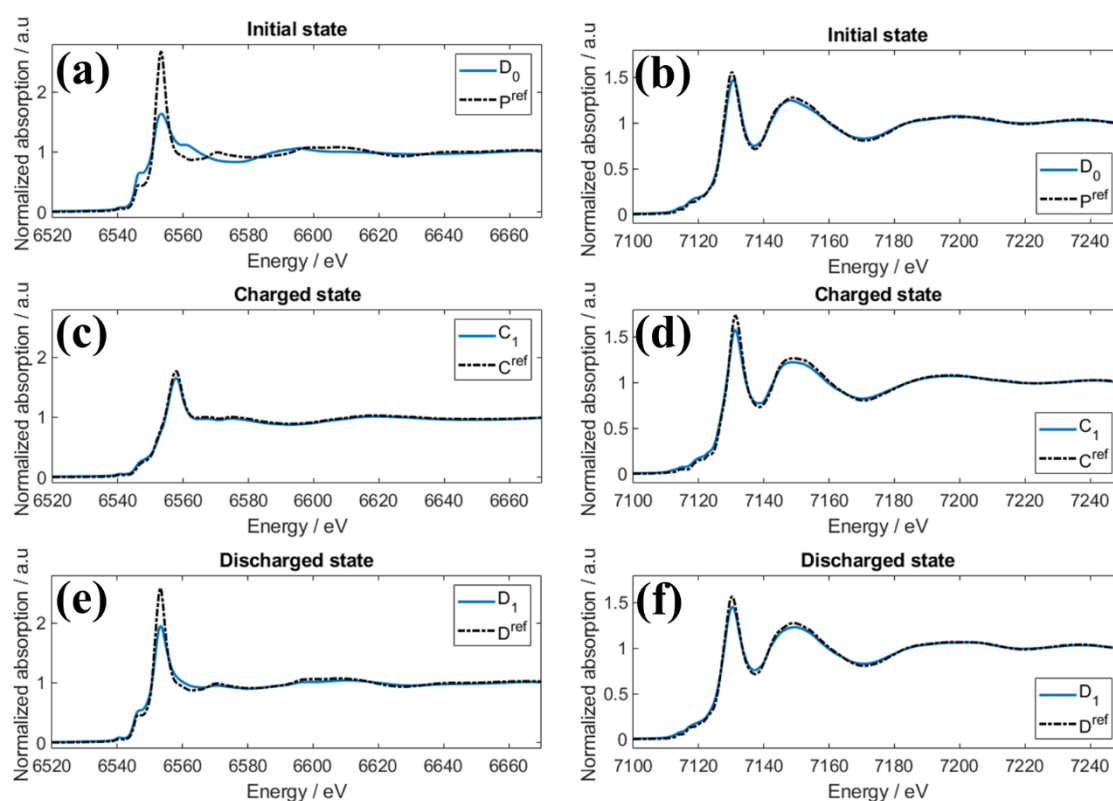


Figure 3. Spectra at Mn and Fe K-edges for the initial, charged, and discharged states of charge. Each panel illustrates the comparison of the spectra recorded in the previous work and the ones reported in Reference [11]. The Mn K-edge for the initial, charged, and discharged states is displayed in panels (a), (c), and (e), respectively, while the analog series at the Fe K-edge is displayed in panels (b), (d), and (f).

3.3. Operando XANES and MCR-ALS Data Analysis

The operando dataset recorded during charge (from spectrum 4 $\equiv D_0$ to spectrum 64 $\equiv C_1$) and discharge (from spectrum 65 to spectrum 123 $\equiv D_1$) at the Mn and Fe K-edges is presented in Figure 4. The results point out: (1) the high variability of the Mn K-edge and low modification at the Fe K-edge; (2) the energy shift occurring at both Mn and Fe sites during charge (shift towards higher energies up to C_1 state of charge) and discharge (shift towards lower energies up to D_1 state of charge). The large dataset acquired at both edges was analyzed with the MCR-ALS chemometric approach, revealing the three pure spectral components necessary to describe the electrochemical cycling processes in the present case study and the concentration profile plot for each component.

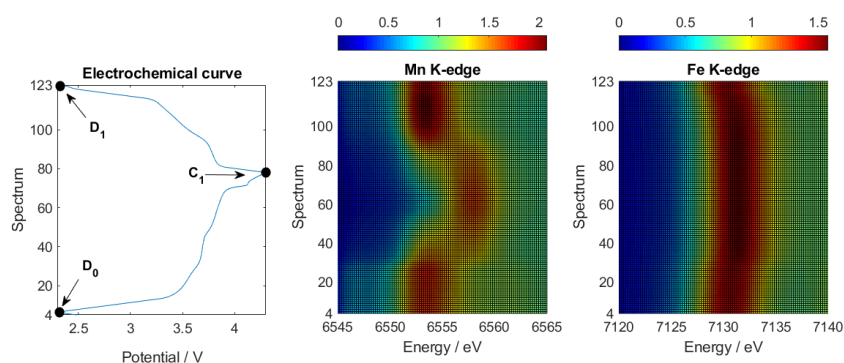


Figure 4. X-ray absorption fine structure (XAFS) operando dataset at the Mn and Fe K-edges and the respective electrochemical curve.

According to the PCA analysis (cf. SI), a minimum of three different pure spectral components is necessary to interpret the complete set of data at both edges. The unique components describing the whole cycling process are presented in Figure 5a,b for Mn and Fe, respectively, while the corresponding concentration profile plots are reported in Figure 5c,d. Contrary to what has been already reported for the same system under the conventional charge/discharge cycling protocol [12], the initial state Mn (D_0) is not uniquely described by a single component, i.e., “Component 1”, but also by an additional contribution, labeled “Component 2”, which accounts for 10% in D_0 (cf. Panels a,c). Due to the mixed character observed for D_0 , the respective spectrum does not match the P^{ref} spectrum in Figure 3a. The electrochemical protocol here adopted induces the formation of a new spectral component (Component 2) already in D_0 , which, during charge, reaches a maximum in concentration around spectrum 35 for both sets of data (cf. Panels c,d). Despite the presence of mixed contributions in the initial state and during charge, Component 3 completely represents the fully charged state (C_1) at both edges, in line with the comparison and good agreement with C^{ref} spectra in Figure 3c,d. During the following discharge, pure spectral Component 1 and Component 2 rise at the expense of the third one, which tends to disappear in the fully discharged state. Component 2 is present in a relatively wide range of spectra (i.e., states of charge), largely persisting in D_1 . On the other hand, the Fe in D_1 almost entirely consists of Component 1 as the initial state, i.e., Fe $D_0 \sim$ Fe D_1 . The discrepancy between Mn D_0 and Mn D_1 states, already visible from Figure 2, is confirmed by the MCR-ALS analysis and attributed to the anomalous charge/discharge protocol to which the cell was subjected.

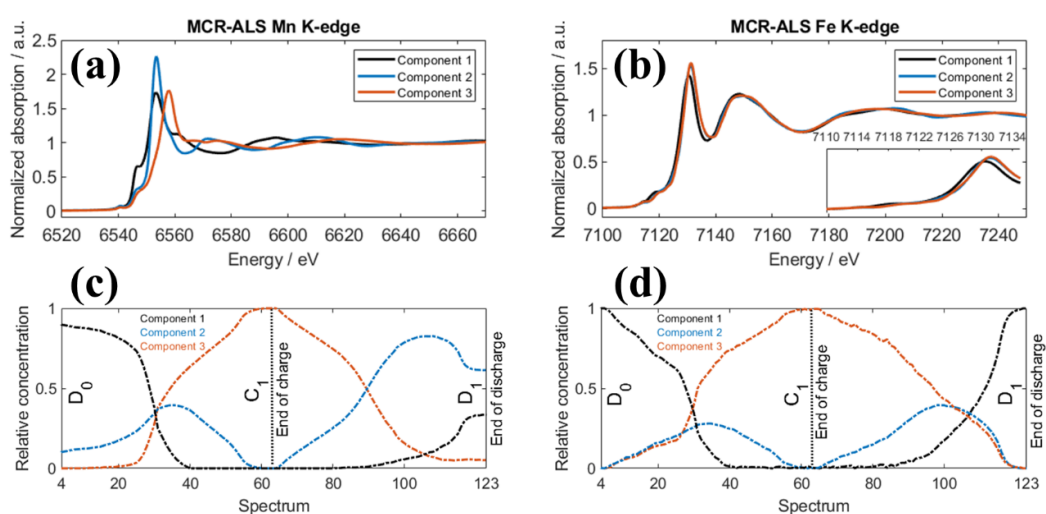


Figure 5. Multivariate Curve Resolution—Alternating Least Square (MCR-ALS) retrieved pure spectral components at the (a) Mn and (b) Fe K-edges and respective concentration profile plots (c,d).

3.4. EXAFS

To shed light on the nature of Component 2, the analysis of the EXAFS portion of the XAFS spectra was performed to provide relevant structural information. The local structure of MnHCF was refined for the most relevant states of charge, i.e., D_0 , C_1 , and D_1 , considering all three components retrieved by the MCR-ALS analysis. Table 1 reports all of the most relevant fitting parameters for the fitted signals, while Figure 6 displays the experimental Fourier transform signals and the respective calculated ones, together with a pair of contour plots as examples for the error parameter determination. By taking into account the results of the MCR-ALS analysis and the agreement with the earlier spectra in Figure 3, the Mn–N ligation was differently considered—in the starting structural model used for the fitting—depending on the mixed character of the Mn state of charge. For this reason, an asymmetric environment for the Mn site, i.e., a distorted octahedron characterized by four equivalent equatorial Mn–N_{eq} and two equivalent axial Mn–N_{ax}, was adopted for D_0 . C_1 state and Component 3, which well describes the Mn local structure in this state, were fitted by considering an asymmetric MnN₆ octahedron due to the expected formal trivalent oxidation state of Mn and the respective JT distortion [11–13]. D_1 , instead, is well described by symmetric Mn–N coordination, in line with the occurrence of divalent Mn ions, as a result of the reduction of MnHCF and the Li-ion uptake. The complete match of the experimental versus the theoretical curves of Figure 6 fitting proves the reliability of the above-mentioned structural models used for the data analysis. The EXAFS fitting results indicate: (i) C_1 is structurally similar to Component 3, with the Fe–C, C ≡ N, Mn–N_{eq}, and Mn–N_{ax} pair distance values equal to 1.89, 1.17, 1.98, and 2.18–2.19 Å, respectively. In addition, they are very close to those reported for ex-situ and in-situ measurements on charged manganese hexacyanoferrate [11,12]. The same holds for their relative EXAFS Debye-Waller Factor. (ii) D_0 is structurally similar to Component 1, considering the same parameters described above, but both are very different with respect to the pristine material, especially when considering the Mn local environment [11,12]. A large difference affects the Mn site, where the Mn–N distance quotation of 2.18 Å usually found for the pristine material [11,12] splits to 2.10 Å and 2.34–2.35 Å; (iii) Component 2 is characterized by an asymmetric distribution of the Mn–N first shell: four Mn–N_{eq} at 2.10 Å and two Mn–N_{ax} at 2.17 Å. The differences in equatorial/axial Mn–N bond lengths are lower than the respective values in Component 1, where the variation amounts to 0.26 Å.

Table 1. Relevant extended X-ray absorption fine structure (EXAFS) refined parameters for the D_0 , C_1 , and D_1 states of charge, as well as the three components retrieved by the MCR-ALS analysis.

	D_0	C_1	D_1	Component 1	Component 2	Component 3
Fe–C/Å	1.857(3)	1.894(6)	1.878(2)	1.864(2)	1.900(2)	1.895(2)
σ^2 Fe–C/Å ²	0.0031(5)	0.0033(5)	0.0027(4)	0.0022(2)	0.0030(4)	0.0029(5)
C≡N/Å	1.190(6)	1.172(7)	1.181(2)	1.187(2)	1.172(3)	1.170(3)
σ^2 C≡N/Å ²	0.005(1)	0.009(1)	0.0087(5)	0.005(1)	0.012(1)	0.007(1)
Mn–N _{eq} /Å	2.10(2)**	1.98(2)**	2.150(4)*	2.09(1)**	2.10(1)**	1.986(6)**
σ^2 Mn–N _{eq} /Å ²	0.010(2)	0.008(2)	0.011(2)	0.010(1)	0.002(1)	0.008(2)
Mn–N _{ax} /Å	2.34(2)***	2.19(2)***	/	2.35(2)***	2.17(1)***	2.18(1)***
σ^2 Mn–N _{ax} /Å ²	0.018(5)	0.018(3)	/	0.014(3)	0.014(4)	0.018(3)
σ^2 Fe–C–N/deg ²	12(5)	14(8)	44(20)	19(5)	16(10)	9(5)
σ^2 Mn–N–C/deg ²	4(3)	4(3)	4(3)	4(3)	28(15)	4(3)
θ Fe–C–N/deg	180	180	180	180	180	180
θ Mn–N–C/deg	180	180	180	180	180	180
E_0 Mn	6540(1)	6546(1)	6542.4(8)	6540(1)	6541(2)	6547.6(8)
E_0 Fe	7116.1(6)	7117.7(4)	7117.4(2)	7116.6(3)	7117.7(5)	7117.8(5)
S^2 Mn	0.65(3)	0.65(3)	0.65(3)	0.65(3)	0.65(3)	0.65(3)
S^2 Fe	0.80(3)	0.80(3)	0.80(3)	0.80(3)	0.80(3)	0.80(3)
χ^2 -like residual/(10 ⁻⁶)	1.29	1.38	2.65	4.76	7.53	4.26

* CN = 6. ** CN = 4. *** CN = 2. CN = coordination number.

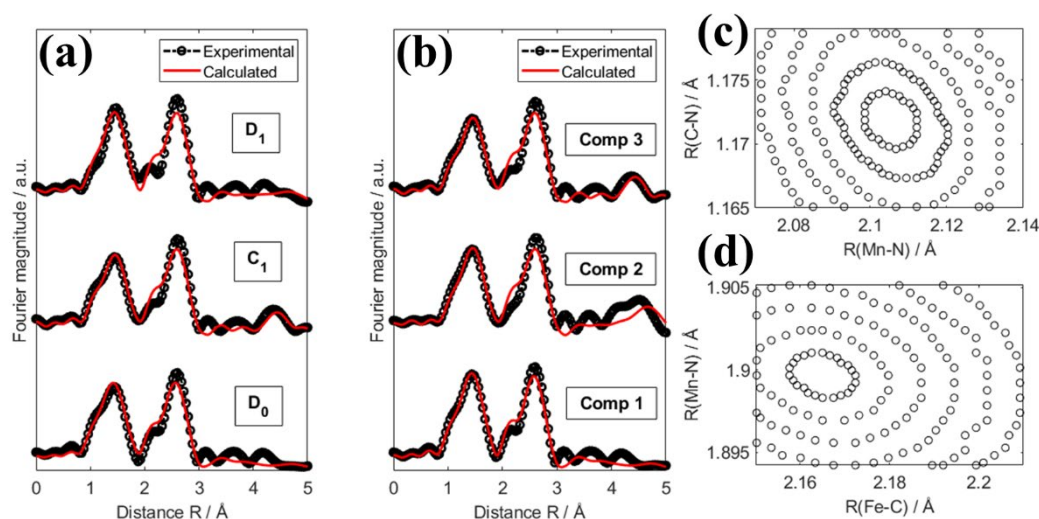


Figure 6. EXAFS fitting analysis on (a) the most relevant states of charge, i.e., D_0 , C_1 , and D_1 , as well as (b) all three components retrieved by the MCR-ALS analysis. The experimental Fourier transform signal is compared to the calculated one in all instances. (c,d) Examples of contour plots for the error parameter determination. These refer to highly correlated parameters; the inner elliptical circle corresponds to a 95% confidence level.

4. Discussion

Manganese hexacyanoferrate material is being considered as a potential alternative to traditional chemistries for large-scale rechargeable batteries. The adopted electrochemical protocol aims at simulating BMS malfunctioning and investigating the structural and chemical effects on manganese hexacyanoferrate. Although the electrochemical efficiency for the first cycle results was significantly affected, the overall local structural environment around each photo absorber, i.e., Mn and Fe, was not severely damaged. The state of charge after the protocol differs from the pristine state as expected and consists of an additional spectral contribution, labeled “Component 2” in the MCR-ALS analysis. The charge state C_1 and Component 3 (from the MCR-ALS analysis) were both fitted by considering an asymmetric Mn-environment because of the trivalent oxidation state of Mn and the respective JT distortion. MCR-ALS suggests that Component 2 is not exclusively present during cycling. However, the identification of the spectrum of the pure component allowed an EXAFS analysis; the differences in equatorial/axial Mn–N bond lengths are reduced when compared to Component 1, where the respective difference amounts to 0.26 Å. The protocol has, therefore, both an electrochemical and structural effect on the system, especially at the beginning of the cycling. The eventual recovery of electrochemical performance after a BMS malfunction is of great importance for technological applications and needs to be further explored, for long-term cycling as well.

Supplementary Materials: The following are available online at www.mdpi.com/2076-3417/10/21/7573/s1: Figure S1: Current density profile.; Figure S2: Magnification of the spectra at the Fe K-edge for D_0 , C_1 , and D_1 states of charge; Figure S3: Magnification of the comparison between the spectra at the Fe K-edge for the initial, charged, and discharged states of charge; Figure S4: PCA analysis highlights the need to use at least 3 different spectral components to describe entirely both datasets.

Author Contributions: Conceptualization, M.G., S.P., and A.M.; methodology, M.G. and A.M.; investigation—X-ray absorption spectroscopy measurements, A.M., S.B., L.S., and M.G.; data curation—MCR-ALS, L.S.; data curation—EXAFS analysis, M.G.; data curation—XANES analysis, A.M.; writing—original draft preparation, A.M. and M.G.; writing—review and editing, all authors; funding acquisition, M.G., L.S., and S.P. All authors have read and agreed to the published version of the manuscript.

Funding: This research was funded by the University of Bologna, RFO Funding (M.G.) and by the Synchrotron SOLEIL through project #20171297. The HIU authors acknowledge the basic funding of the Helmholtz Association.

Acknowledgments: This work was supported by a public grant overseen by the French National Research Agency (ANR) as part of the “Investissements d’Avenir” program (reference: ANR10-EQPX45).

Conflicts of Interest: The authors declare no conflicts of interest.

References

1. Reddy, M.V.; Mauger, A.; Julien, C.M.; Paoletta, A.; Zaghbi, K. Brief History of Early Lithium-Battery Development. *Materials (Basel)* **2020**, *13*, 1884.
2. Xie, J.; Lu, Y. A retrospective on lithium-ion batteries. *Nat. Commun.* **2020**, *11*, 2499.
3. *United Nations Sustainable Development—17 Goals to Transform Our World*; United Nations: New York, NY, USA, 2015.
4. Abada, S.; Marlair, G.; Lecocq, A.; Petit, M.; Sauvant-Moynot, V.; Huet, F. Safety focused modeling of lithium-ion batteries: A review. *J. Power Sources* **2016**, *306*, 178–192.
5. Omariba, Z.; Zhang, L.; Sun, D. Review on Health Management System for Lithium-Ion Batteries of Electric Vehicles. *Electronics* **2018**, *7*, 72.
6. Ali, M.U.; Zafar, A.; Nengroo, S.H.; Hussain, S.; Alvi, M.J.; Kim, H.-J. Towards a Smarter Battery Management System for Electric Vehicle Applications: A Critical Review of Lithium-Ion Battery State of Charge Estimation. *Energies* **2019**, *12*, 446.
7. Tran, M.K.; Fowler, M. A review of lithium-ion battery fault diagnostic algorithms: Current progress and future challenges. *Algorithms* **2020**, *13*, 62.
8. Paoletta, A.; Faure, C.; Timoshevskii, V.; Marras, S.; Bertoni, G.; Guerfi, A.; Vijn, A.; Armand, M.; Zaghbi, K. A review on hexacyanoferrate-based materials for energy storage and smart windows: Challenges and perspectives. *J. Mater. Chem. A* **2017**, *5*, 18919–18932.
9. Wang, B.; Han, Y.; Wang, X.; Bahlawane, N.; Pan, H.; Yan, M.; Jiang, Y. Prussian Blue Analogs for Rechargeable Batteries. *iScience* **2018**, *3*, 110–133.
10. Moritomo, Y.; Takachi, M.; Kurihara, Y.; Matsuda, T. Synchrotron-Radiation X-Ray Investigation of Li + /Na + Intercalation into Prussian Blue Analogues. *Adv. Mater. Sci. Eng.* **2013**, *2013*, 967285.
11. Mullaliu, A.; Asenbauer, J.; Aquilanti, G.; Passerini, S.; Giorgetti, M. Highlighting the Reversible Manganese Electroactivity in Na-Rich Manganese Hexacyanoferrate Material for Li- and Na-Ion Storage. *Small Methods* **2020**, *4*, 1900529.
12. Mullaliu, A.; Aquilanti, G.; Conti, P.; Giorgetti, M.; Passerini, S. Effect of Water and Alkali-Ion Content on the Structure of Manganese(II) Hexacyanoferrate(II) by a Joint Operando X-ray Absorption Spectroscopy and Chemometric Approach. *ChemSusChem* **2020**, *13*, 608–615.
13. Mullaliu, A.; Gaboardi, M.; Plaisier, J.R.; Passerini, S.; Giorgetti, M. Lattice Compensation to Jahn–Teller Distortion in Na-Rich Manganese Hexacyanoferrate for Li-Ion Storage: An Operando Study. *ACS Appl. Energy Mater.* **2020**, *3*, 5728–5733.
14. Leriche, J.-B.; Hamelet, S.; Shu, J.; Morcrette, M.; Masquelier, C.; Ouvrard, G.; Zerrouki, M.; Soudan, P.; Belin, S.; Elkaïm, E.; et al. An Electrochemical Cell for Operando Study of Lithium Batteries Using Synchrotron Radiation. *J. Electrochem. Soc.* **2010**, *157*, A606–A610.
15. Briois, V.; La Fontaine, C.; Belin, S.; Barthe, L.; Moreno, T.; Pinty, V.; Carcy, A.; Girardot, R.; Fonda, E. ROCK: The new Quick-EXAFS beamline at SOLEIL. *J. Phys. Conf. Ser.* **2016**, *712*, 012149.
16. Ravel, B.; Newville, M. ATHENA, ARTEMIS, HEPHAESTUS: Data analysis for X-ray absorption spectroscopy using IFEFFIT. *J. Synchrotron Rad.* **2005**, *12*, 537–541.
17. de Juan, A.; Jaumot, J.; Tauler, R. Multivariate Curve Resolution (MCR). Solving the mixture analysis problem. *Anal. Methods* **2014**, *6*, 4964.
18. Fehse, M.; Iadecola, A.; Sougrati, M.T.; Conti, P.; Giorgetti, M.; Stievano, L. Applying chemometrics to study battery materials: Towards the comprehensive analysis of complex operando datasets. *Energy Storage Mater.* **2019**, *18*, 328–337.
19. Filipponi, A.; Di Cicco, A.; Natoli, C.R. X-ray-absorption spectroscopy and n-body distribution functions in condensed matter. I. Theory. *Phys. Rev. B* **1995**, *52*, 15122–15134.
20. Filipponi, A.; Di Cicco, A. X-ray-absorption spectroscopy and n-body distribution functions in condensed matter. II. Data analysis and applications. *Phys. Rev. B* **1995**, *52*, 15135–15149.
21. Giorgetti, M.; Berrettoni, M.; Filipponi, A.; Kulesza, P.J.; Marassi, R. Evidence of four-body contributions in the EXAFS spectrum of Na₂Co[Fe(CN)₆]. *Chem. Phys. Lett.* **1997**, *275*, 108–112.

22. Giorgetti, M.; Berrettoni, M. Structure of Fe/Co/Ni Hexacyanoferrate As Probed by Multiple Edge X-ray Absorption Spectroscopy. *Inorg. Chem.* **2008**, *47*, 6001–6008.
23. Giorgetti, M.; Guadagnini, L.; Tonelli, D.; Minicucci, M.; Aquilanti, G. Structural characterization of electrodeposited copper hexacyanoferrate films by using a spectroscopic multi-technique approach. *Phys. Chem. Chem. Phys.* **2012**, *14*, 5527.
24. Song, J.; Wang, L.; Lu, Y.; Liu, J.; Guo, B.; Xiao, P.; Lee, J.-J.; Yang, X.-Q.; Henkelman, G.; Goodenough, J.B. Removal of Interstitial H₂O in Hexacyanometallates for a Superior Cathode of a Sodium-Ion Battery. *J. Am. Chem. Soc.* **2015**, *137*, 2658–2664.
25. Hedin, L.; Lundqvist, B.I.; Lundqvist, S. Local exchange-correlation potentials. *Solid State Commun.* **1971**, *9*, 537–541.
26. Krause, M.O.; Oliver, J.H. Natural widths of atomic K and L levels, K α X-ray lines and several K L L Auger lines. *J. Chem. Phys. Ref. Data* **1979**, *8*, 329–338.

Publisher's Note: MDPI stays neutral with regard to jurisdictional claims in published maps and institutional affiliations.



© 2020 by the authors. Licensee MDPI, Basel, Switzerland. This article is an open access article distributed under the terms and conditions of the Creative Commons Attribution (CC BY) license (<http://creativecommons.org/licenses/by/4.0/>).